International Journal of Fatigue 193 (2025) 108746

Contents lists available at ScienceDirect

International Journal of Fatigue

journal homepage: www.elsevier.com/locate/ijfatigue

Effect of Inconel 625 coating via high-speed laser direct energy deposition on the fatigue characteristics of Q235 steel

Cheng Zhong [a], Peng Liu [a], Xuechong Ren [a,b,*], Benli Luan [c,d,*], Alex A. Volinsky [e]

[a] National Center for Materials Service Safety, University of Science and Technology Beijing, Beijing 100083, China
[b] State Key Laboratory of Nuclear Power Safety Technology and Equipment, University of Science and Technology Beijing, Beijing 100083, China
[c] Eastern Institute for Advanced Study, Eastern Institute of Technology, Ningbo, Zhejiang 315200, China
[d] Department of Chemistry, Western University, London, Ontario N6A 5B7, Canada
[e] Department of Mechanical Engineering, University of South Florida, 4202 E. Fowler Ave. ENG030, Tampa FL 33620, USA

ARTICLE INFO

Keywords:
High-speed laser direct energy deposition
Inconel 625 coating
Tensile
Fatigue
Corrosion

ABSTRACT

Single-layer and double-layer Inconel 625 coatings were deposited on the Q235 steel using high-speed laser direct energy deposition (HL-DED). Steel grains in heat-affected zone (HAZ) coarsened due to the heat generated during the single-layer coating deposition. In contrast, double-layer coating specimens exhibited fine-grain regions in the HAZ due to repeated laser treatment reaching the solid-state phase transition temperature. Compared to bare Q235 steel, the yield and ultimate tensile strength of the single-layer coated specimens increased by 25% and 21%, respectively, while their elongation decreased by 32%. Tensile strength increased, while elongation decreased with the coating thickness. Although fatigue performance of bulk HL-DED Inconel 625 and as-deposited coating specimens was lower than bare Q235 steel, polished coated specimens exhibited better fatigue performance than bare Q235 steel. The coating thickness in the as-deposited condition had minimal impact on fatigue performance, but the fatigue performance of the polished coated specimens decreased with coating thickness. Corrosion fatigue life of the single-layer coated specimens in a 3.5% NaCl solution was three times better than bare Q235, and the fatigue life of double-layer coated specimens is not affected by the corrosive environment.

1. Introduction

Mild steel is extensively used in marine engineering due to its excellent mechanical properties and cost-effectiveness [1]. However, mild steel has poor corrosion resistance and easily corrodes in marine environments, which affects its fatigue life and reliability [2,3]. In contrast, Inconel 625 alloy has exceptional corrosion resistance, especially in seawater, but its high cost limits large-scale marine applications [4–7]. To combine the mechanical properties of mild steel with the corrosion resistance of Inconel 625, researchers have investigated surface modification techniques to prepare corrosion-resistant coatings on mild steel to enhance its corrosion resistance without compromising mechanical properties.

Laser cladding is an advanced surface modification technology that has high precision and controllability combined with excellent coating adhesion [8]. However, the process has low efficiency and significant thermal impact on the substrate limits its industrial applications. High-speed laser direct energy deposition (HL-DED) is an improvement of traditional laser-powder coupling methods and utilizes higher laser energy to melt the powder for producing the coating. This significantly enhances deposition efficiency combined with lower substrate temperature [9,10].

Numerous studies over the past decades have demonstrated that laser cladding Inconel 625 coatings exhibit superior corrosion resistance in chloride-containing aqueous environments [11–15]. Yet, laser cladding process causes thermal damage to the substrate and introduces defects in the coating such as pores, cracks, and poor adhesion, significantly compromising fatigue performance [16,17]. Residual stresses induced by laser cladding in the coating and the substrate can also reduce fatigue life, and the fatigue performance cannot be improved through stress-relieving annealing treatments [18]. The differences between the coating and the substrate properties and structure are the key factors reducing fatigue life of the coated specimens compared to the substrate material [19]. Coatings promote fatigue crack initiation,

* Corresponding authors.
E-mail addresses: xcren@ustb.edu.cn (X. Ren), bluan@uwo.ca (B. Luan).

https://doi.org/10.1016/j.ijfatigue.2024.108746
Received 31 July 2024; Received in revised form 31 October 2024; Accepted 29 November 2024
Available online 1 December 2024

Table 1
Chemical composition of the Inconel 625 powder and Q235 steel in wt.%.

Material	Al	Co	Cr	Mo	Nb	Mn	C	Si	Fe	Ni
Inconel 625	0.2	0.07	22.17	8.46	3.36	0.21	0.056	0.31	4.03	Balance
Q235 steel						0.4	0.2	0.3	Balance	

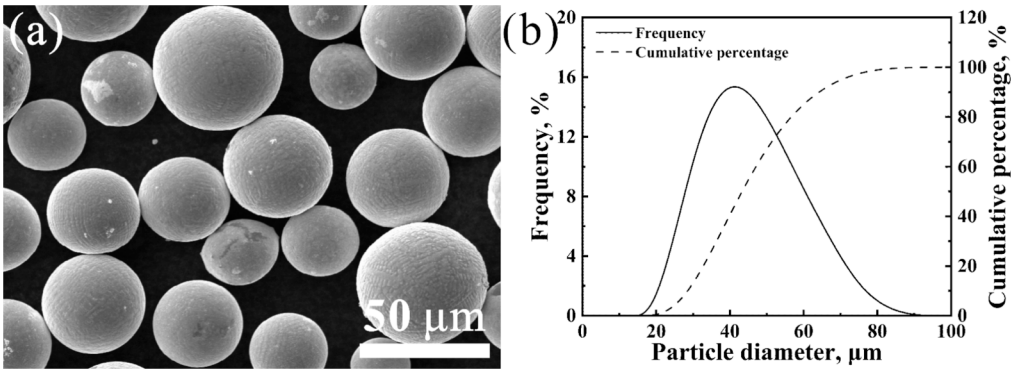

Fig. 1. (a) Scanning electron microscopy image of the Inconel 625 powder; (b) Powder particle size distribution.

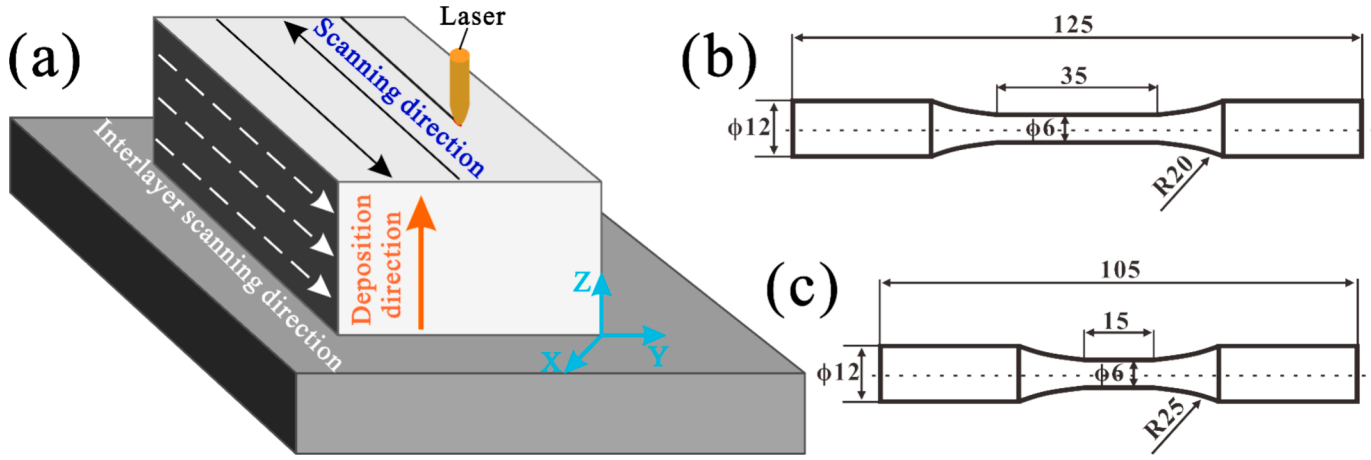

Fig. 2. (a) Bulk HL-DED Inconel 625 manufacturing process schematics; (b) Bulk HL-DED Inconel 625 tensile specimen dimensions in mm; (c) Bulk HL-DED Inconel 625 fatigue specimen dimensions in mm.

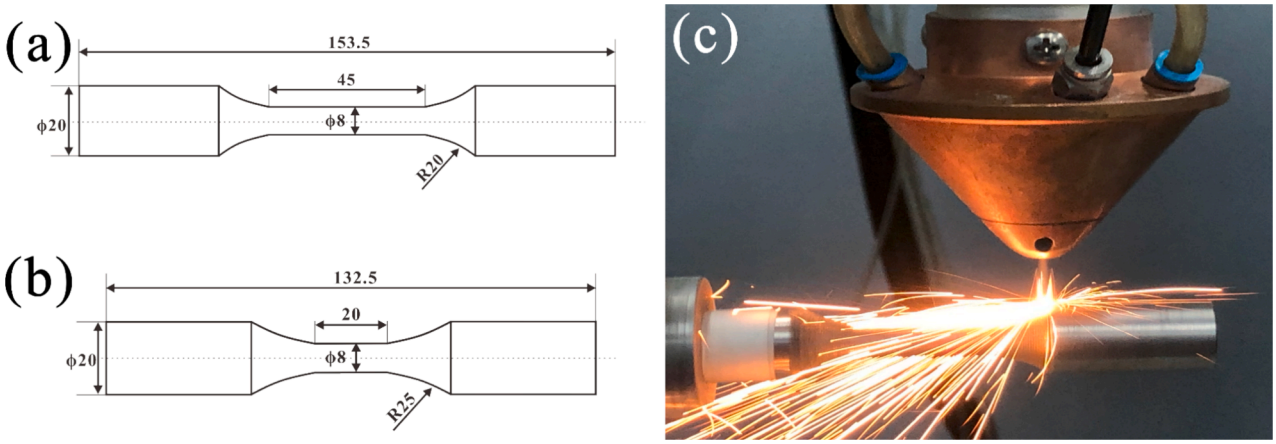

Fig. 3. (a) Tensile specimen dimensions in mm; (b) Fatigue specimen dimensions in mm; (c) Photograph of the Inconel 625 coating deposition on rotating Q235 steel.

Table 2
HL-DED Inconel 625 coating process parameters.

Rotation frequency Laser power	3 Hz	3.8 Hz	4.6 Hz
1.6 kW	Specimen 1	Specimen 2	Specimen 3
1.8 kW	Specimen 4	Specimen 5	Specimen 6
2 kW	Specimen 7	Specimen 8	Specimen 9

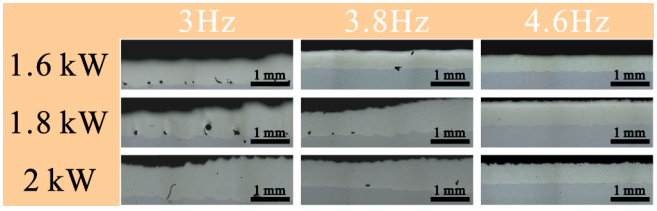

Fig. 4. Optical images of the transverse-section of HL-DED Inconel 625 coating deposited at different process parameters.

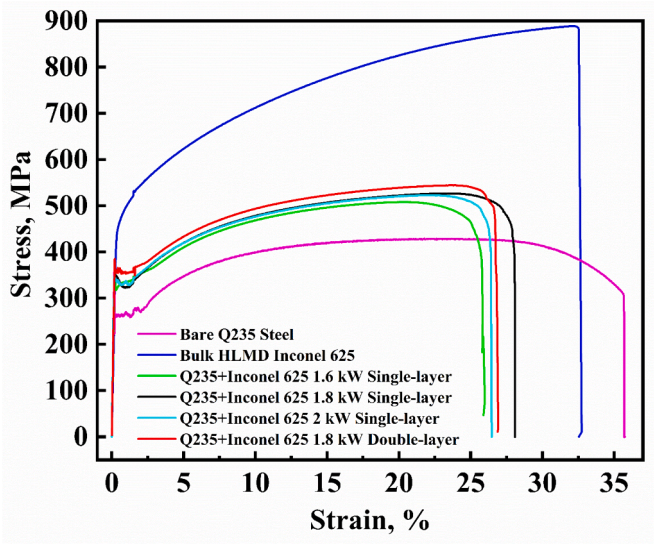

Fig. 5. Representative strain–stress curves for the different specimens.

Table 3
Tensile test results of bare Q235 steel, bulk HL-DED Inconel 625 and coated specimens.

Specimens	YS, MPa	UTS, MPa	Elongation, %
Bare Q235 steel	264 ± 5	429 ± 3	35 ± 1
Bulk HL-DED Inconel 625	465 ± 9	890 ± 11	28 ± 1
Q235 + Inconel 625 1.6 kW Single-layer	321 ± 6	502 ± 4	23.5 ± 1
Q235 + Inconel 625 1.8 kW Single-layer	332 ± 10	520 ± 5	23.5 ± 1
Q235 + Inconel 625 2 kW Single-layer	321 ± 10	521 ± 4	21.5 ± 3
Q235 + Inconel 625 1.8 kW Double-layer	354 ± 6	546 ± 2	21.5 ± 1

thereby reducing fatigue life [20]. Thicker coatings lead to larger size and number of defects in the coating, also resulting in reduced fatigue life [21]. Thinner coatings are better for improving fatigue life compared with thicker coatings. However, another study suggested that thicker Inconel 625 coatings on AISI 304L steel exhibited improved fatigue life compared to thinner coatings [22]. The Inconel 625 coating on the AISI 316L surface resulted in the formation of finer dendrites within the coating, thus enhancing the substrate fatigue life [23]. Laser cladding Inconel 625 coating increased fatigue life of the 42CrMo steel at high-stress levels, but diminished it under low-stress levels [16].

Currently there is no consensus regarding the effectiveness of laser cladding coatings in improving the fatigue characteristics of substrate materials. While HL-DED technology improves coating deposition efficiency, the impact of HL-DED Inconel 625 coating on the fatigue behavior of Q235 steel remains unclear. This study systematically investigates, for the first time, the effects of HL-DED Inconel 625 coatings on the microstructure and fatigue properties of Q235 steel, along with the impact of corrosion on fatigue characteristics. Comprehensive analysis of microstructure, microhardness, tensile properties, fatigue behavior, and fracture surface of coated specimens is presented. This research addresses gaps in the literature and provides crucial insights to support future industrial applications of corrosion-resistant alloy coatings fabricated by HL-DED.

2. Material and methods

2.1. Specimens preparation

Inconel 625 spherical powder from Sailong Metal Company (China) were used for the bulk HL-DED Inconel 625 and coated specimens. The chemical composition of the powders is listed in Table 1. The powders are mostly spherical with smooth surfaces in Fig. 1(a). Fig. 1(b) shows the particle size distribution measured by a laser particle size analyzer. The powders were dried in an oven at 100 ℃ for 120 min to ensure good fluidity and to remove moisture [24].

Bulk HL-DED Inconel 625 and coated specimens were manufactured using the ultra-high-speed laser cladding system (ZKZM-4000, ZKZM Co., China), which includes 4 kW laser, a central powder feeding system, and a computer numerical control stage. Bulk HL-DED Inconel 625 manufacturing process schematics are shown in Fig. 2(a). The deposition parameters were 1.8 kW laser power, 22 g/min powder feeding rate, 4 m/min laser scanning velocity, 80 % deposition tracks overlap, and 0.5 mm interlayer elevation [24]. Tensile and fatigue properties were tested along the Y direction with the corresponding samples' geometry presented in Fig. 2(b) and (c).

The substrate material for HL-DED Inconel 625 coatings was hot-rolled Q235 steel cut into cylinders with a 20 mm diameter. The Q235 steel chemical composition is listed in Table 1. Before deposition, the Q235 steel specimens were machined into the geometrical shapes shown in Fig. 3(a) and (b), following the GB/T 228.1–2010 and GB/T 3075–2008 standards [25,26]. The photograph taken during the HL-DED Inconel 625 coating deposition is presented in Fig. 3(c). In coating deposition, laser power and deposition rate significantly affect quality [27]. Therefore, adjusting laser power and deposition rate while keeping other parameters is a common and efficient approach to optimize the coating process [28]. During deposition, the laser beam was moved along the cylindrical steel sample length to produce clad tracks with 80 % overlap. The powder feeding rate was 34 g/min. The laser power was varied along with the rotation frequency, as listed in Table 2. Although higher rotation speeds improve coating preparation efficiency, the maximum frequency of the computer numerical control equipment is limited to 5 Hz. A single-layer Inconel 625 coating was produced moving the laser beam from left to right, while the double-layer coating was produced by laser beam passed from left to right, and then from right to left. For the double-layer coating, the endpoint of the first layer deposition served as the starting point for the second layer deposition. Based in the Inconel 625 coating defects and tensile properties discussed later, the optimal deposition parameters were 1.8 kW laser power and 4.6 Hz rotation frequency.

2.2. Microstructure Characterization

Metallographic specimens were obtained from the center of the

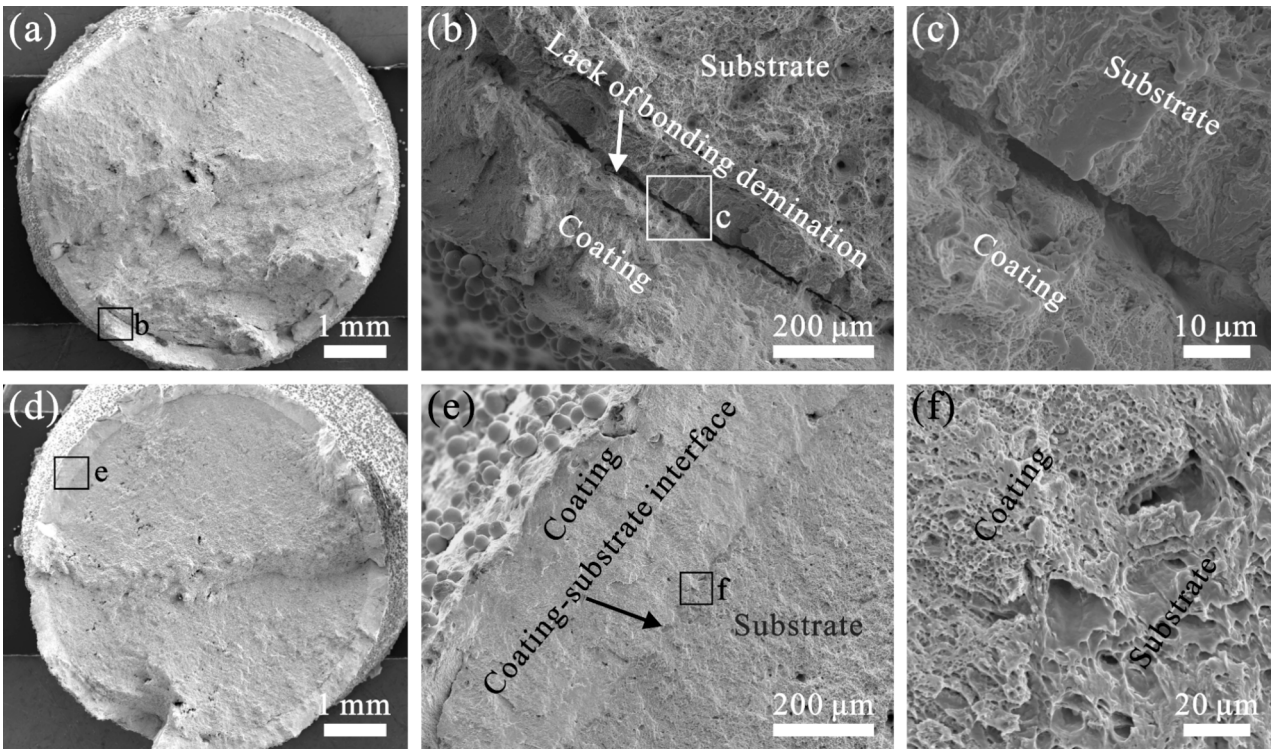

Fig. 6. Tensile fracture surfaces of single-layer coated specimens deposited at (a-c) 1.6 kW laser power; (d-f) 1.8 kW laser power.

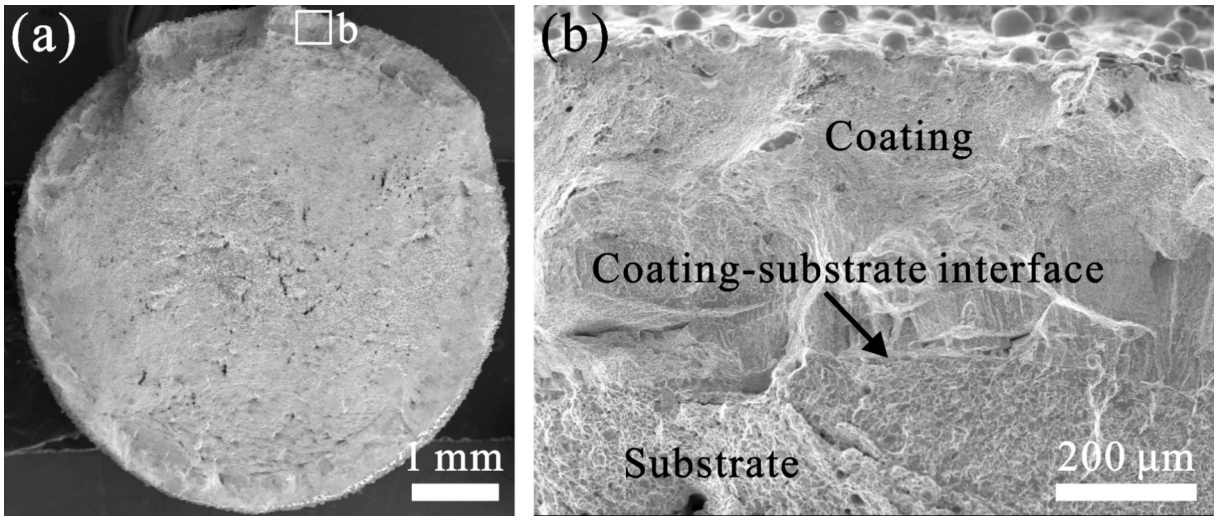

Fig. 7. Tensile fracture surface of the 1.8 kW double-layer coated specimen: (a) The whole sample and (b) Magnified coating-substrate interface.

coated specimen along the transverse-section cut parallel to the specimen length using electrical discharge machining. They were sequentially ground with 600 to 3,000 grits SiC paper and polished to a fine finish with a 1 μm diamond suspension. Polished specimens were etched in a 4 % Nital solution (4 % nitric acid and 96 % ethanol) for 6 sec in the Q235 steel area, and electrolytically etched with a 10 % oxalic acid and 90 % deionized water solution for 8 sec at 3 V in Inconel 625 coating area. Microstructure investigations were performed using an optical microscope (OLYMPUS BX53M) and a field-emission scanning electron microscope (SEM, ZEISS SUPRA55). Elemental composition analysis was conducted using an electron probe microanalyzer (EPMA, JXA-8530F-Plus). Electron backscatter diffraction (EBSD) was employed to examine the grain morphology of the coated specimens. The EBSD specimen was polished to a mirror-like surface following metallographic preparation standards and electropolished using a DC power supply at 30 V for 10 sec in a solution of 5 % glycerin, 10 % $HClO_4$, and 85 % ethanol. EBSD parameters were set at 20 kV, with measurements taken at a step size of 1 μm.

2.3. Mechanical testing

The microhardness of the coated specimen was evaluated using a QATM Qness 60 A^+ EVO microhardness tester with static indentation. The hardness test was conducted according to standard GBT-27552–2011 [29]. A 200 g load was applied for 15 sec, and the average value was determined from three measurements at the same horizontal height with calculated standard deviation.

Tensile and fatigue tests were carried out using a W + B LFV kN

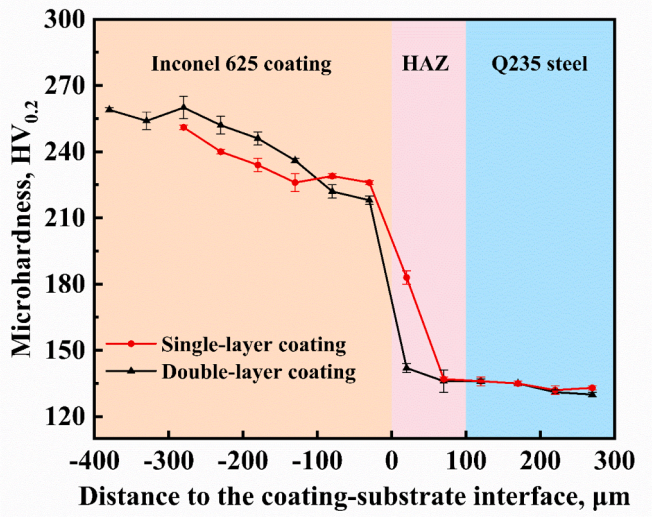

Fig. 8. Transverse-section microhardness variation of single-layer and double-layer coated specimens.

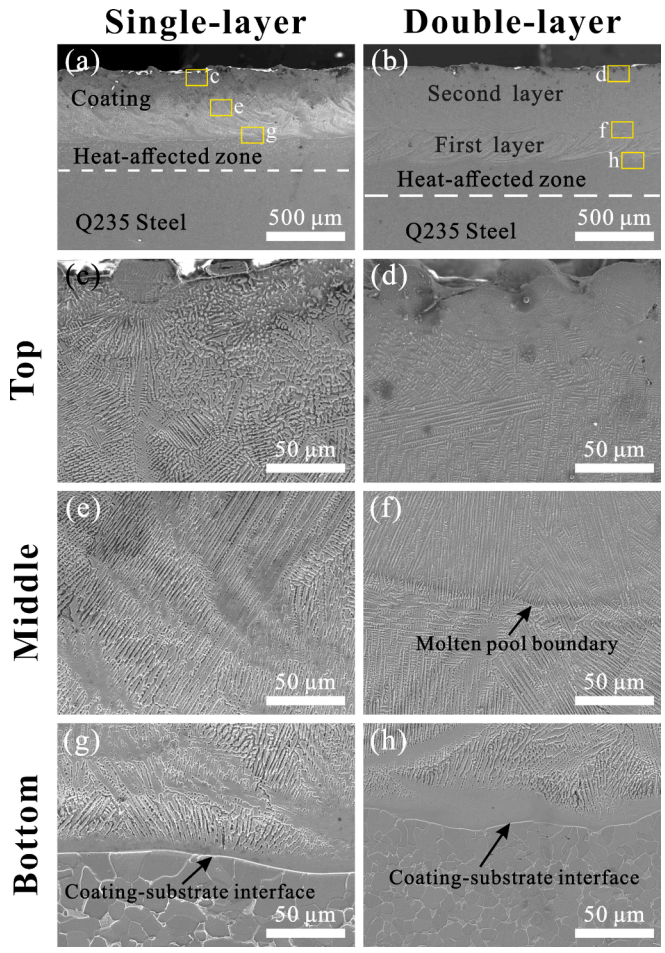

Fig. 9. Single-layer and double-layer coating microstructure of the transverse-section: (a) and (b) Low magnification SEM of the coating and the substrate; (c) and (d) Coating top region; (e) and (f) Coating middle region; (g) and (h) Coating bottom region.

servo-hydraulic universal testing machine equipped with an extensometer. The tensile test was conducted in two stages according to the GB/T 228.1–2010 standard. Initially, strain control was utilized at a rate of 2.5×10^{-3} s^{-1} until the onset of yielding, after which displacement control was set at 1 mm/min. The fatigue test followed the GB/T 3075–2008 standards. Given that many mechanical components experience tension-dominated cyclic loads during operation [23]. Therefore, fatigue tests were conducted under stress control using a sinusoidal waveform with a stress ratio R of 0.1. For high-cycle fatigue, the frequency's effect on test results is negligible below several hundred Hz; thus, a common laboratory frequency of 25 Hz was selected [30]. The fatigue limit was defined as the stress level at which the specimen could endure 5,000,000 cycles without fracture [31]. Corrosion fatigue tests were conducted in a 3.5 % NaCl solution with a loading frequency of 10 Hz to allow for adequate corrosion time. This frequency is commonly used in corrosion fatigue testing [32]. Fracture morphology characteristics were observed using SEM.

3. Results and Discussion

3.1. Coating deposition

Various laser deposition process parameters affect the coating quality, including laser power, deposition rate, powder feeding rate, trace overlap, and Ar shielding gas flow rate [33,34]. Among these, laser power and deposition rate have the most significant impact on the coating quality [35,36]. The coating deposition rate is controlled by the rotation frequency in our experiments. Fig. 4 presents optical microscopy images of coatings deposited at different laser power and rotation frequency. Significant debonding occurs in the overlapping regions at 1.6 kW laser power and 3 Hz rotation frequency. This incomplete bonding will reduce the sample's tensile strength [37]. Increasing laser power reduces debonding in the overlapping regions at 3 Hz rotation frequency. However, higher laser power, while beneficial for eliminating debonding defects, also increases the amount of powder melted at each point. This excessive melting accumulates across tracks, resulting in a gradually increasing deposition layer thickness with a sloped profile, as depicted in Fig. 4 for the rotation frequency of 3 Hz and 3.8 Hz.

As the sample rotation frequency increases, the laser beam duration on any given point decreases, reducing the cumulative melted powder volume, which is a contrasting effect to increasing laser power. Consequently, all cladding layers exhibit uniform thickness at 4.6 Hz. The coating thickness does not increase linearly with laser power, and is 318 μm at 1.6 kW, 432 μm at 1.8 kW, and 403 μm at 2 kW for the 4.6 Hz rotation frequency. This discrepancy occurs because 1.8 kW laser power at 34 g/min powder feed is adequate for complete melting. However, at 2 kW, excessive laser power may lead to powder evaporation, thereby reducing the coating thickness. Hence, the coating formed at 2 kW is thinner than at 1.8 kW.

3.2. Tensile and microhardness tests

As depicted in Fig. 4, a defect-free and uniform coating is achieved at 4.6 Hz rotation frequency with 1.6 kW, 1.8 kW, and 2 kW laser power. Tensile specimens were prepared using these three parameters and tested. Fig. 5 displays the representative tensile curves for the various specimens, with detailed test results are summarized in Table 3. The tensile curve indicates that the coated specimen and bare Q235 steel exhibit the same yield plateau, highlighting the substrate's dominant role. The yield strength (YS) and ultimate tensile strength (UTS) of the coated specimens fall between those of bulk HL-DED Inconel 625 and bare Q235 steel. However, the elongation of the coated specimen is lower than both bulk HL-DED Inconel 625 and bare Q235 steel. The improved YS and UTS of the coated specimens can be attributed to the inherent properties of bulk HL-DED Inconel 625, which has higher YS and UTS compared to bare Q235 steel.

The tensile properties of specimens coated at different laser power exhibit significant differences. The YS and UTS of the specimen coated at 1.6 kW is lower than at 1.8 kW and 2 kW, while the specimens coated at

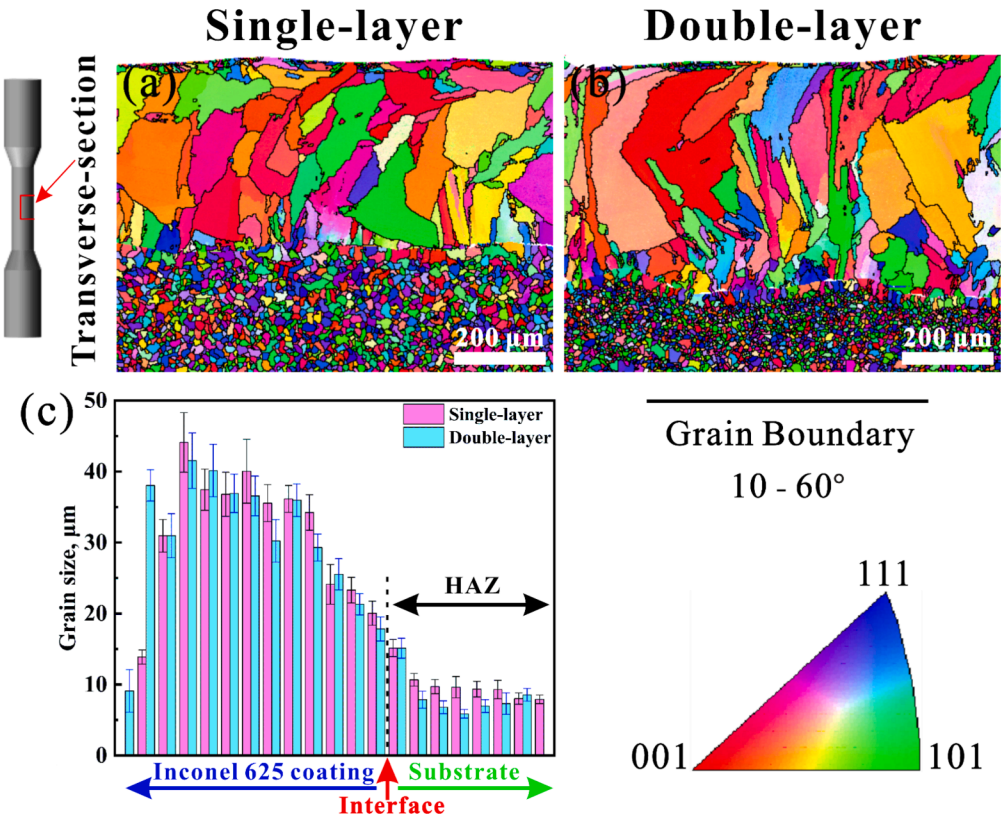

Fig. 10. EBSD results of the coating-substrate transverse-section: (a) Single-layer coated specimen; (b) Double-layer coated specimen and (c) Grain size distribution.

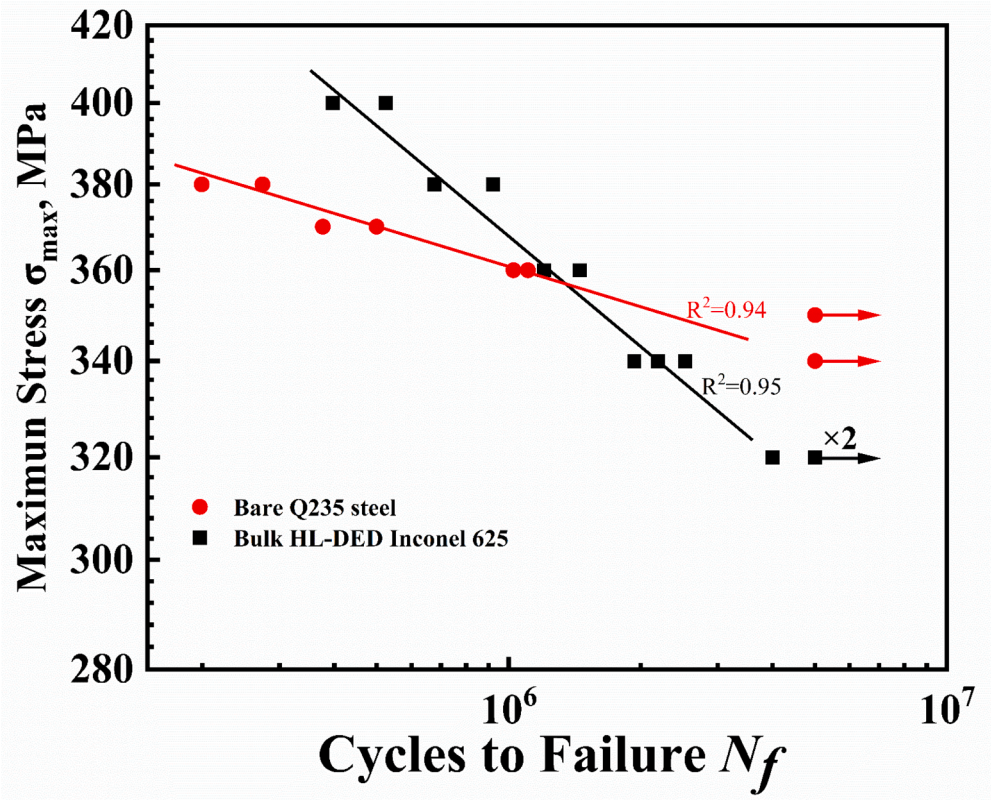

Fig. 11. Fatigue S-N curves for bare Q235 steel and bulk HL-DED Inconel 625 specimens.

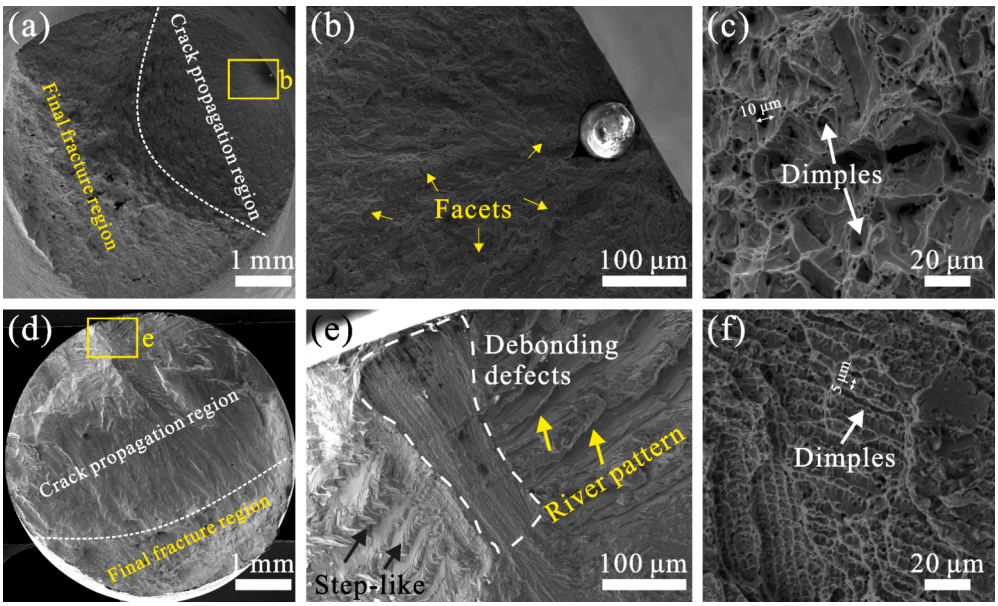

Fig. 12. Fatigue fracture surfaces of specimens tested at σ_{max} = 360 MPa: (a-c) Bare Q235 steel, N_f = 1,036,139; (d-f) Bulk HL-DED Inconel 625, N_f = 1,203,880.

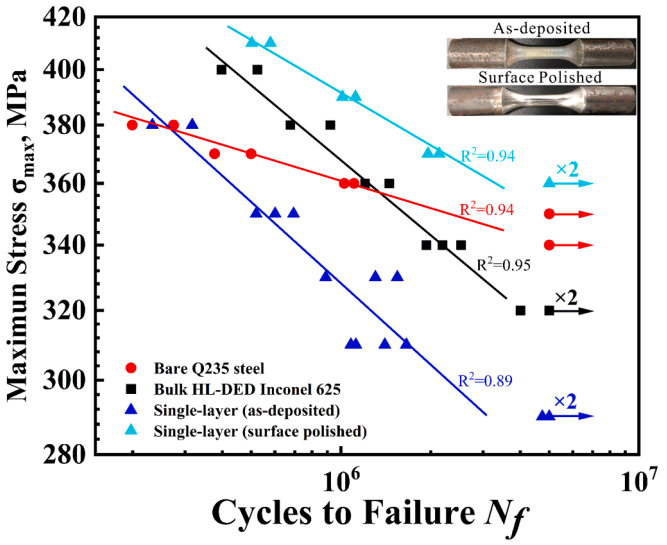

Fig. 13. Fatigue S-N curves for single-layer coated specimens compared to bare Q235 steel and bulk HL-DED Inconel 625 specimens.

l.8 kW and 2 kW demonstrate nearly identical YS and UTS. This can be attributed to the thinner coating of the 1.6 kW specimen. Sample diameter measurements support this observation. The 1.6 kW specimens had a diameter of only 8.48 mm, whereas the 1.8 kW and 2 kW specimens measured 8.64 mm and 8.58 mm, respectively. The coating thickness of the 1.8 kW and 2 kW specimens exhibited minimal variation, resulting in no significant difference in YS and UTS. However, higher laser power results in a larger heat-affected zone (HAZ) in the substrate. Due to temperature gradients and phase changes, significant thermal stresses and brittle phases develop in the HAZ, which reducing the substrate's plasticity [38]. Consequently, the 2 kW specimens show lower elongation compared to the 1.8 kW specimens.

Fig. 6 illustrates the tensile fracture surfaces of single-layer coated specimens deposited at 1.6 kW and 1.8 kW laser power. The tensile fracture primarily consists of dimples, indicating distinct ductile characteristics. Low laser power leads to incomplete bonding between the coating and substrate in Fig. 6(a) and (b), with a clear image of the incomplete bonding feature in Fig. 6(c). The 1.8 kW coated specimen displays a fully bonded and defect-free interface in Fig. 6(d) and (e), with the HAZ exhibiting ductile fracture features characterized by dimples in Fig. 6(f). Additionally, the substrate demonstrates superior plastic deformation capability compared to the coating, enabling greater energy absorption before fracture and resulting in larger dimples.

Based on the above comparative analysis, the 1.8 kW laser power was selected to fabricate double-layer coated specimens. The double-layer coated specimen has a diameter of approximately 8.9 mm. The tensile test results are summarized in Table 3. These double-layer coated specimens demonstrated higher tensile strength compared to single-layer coated specimens. This improvement is primarily attributed to the increased coating thickness. With the coating material having higher strength than the substrate, the overall strength of the coated specimens increases with the coating thickness. Fig. 7(a) shows a low-magnification SEM image of the tensile fracture surface of the 1.8 kW double-layer coated specimen, indicating no obvious defects in the coating, substrate-first layer and the first–second layer interfaces. Fig. 7 (b) is a magnified view of the coating and the substrate, revealing good bonding at both the substrate-first layer and first–second layer interfaces.

Fig. 8 illustrates the microhardness variation across the transverse-section of the single-layer and double-layer coated specimens, from the coating's top to the substrate region. The microhardness gradually decreases from the coating to the substrate. However, there is no significant difference in microhardness between the single-layer and double-layer coated specimens. The maximum hardness of the coating reaches 260 HV, significantly higher than the substrate's hardness of 130 HV. This elevated hardness of the coating is attributed to the formation of fine dendritic structures during the laser cladding process. Similar trends of decreasing microhardness from the coating to the substrate have been observed in other studies of Inconel 625 laser cladding on Q235 steel [39,40].

3.3. Microstructure analysis

Laser deposition is a dynamic process characterized by rapid melting and solidification, which establishes a strong metallurgical bond between the coating and the substrate [41,42]. Fig. 9(a) is a low-magnification SEM image of a single-layer coated specimen, illustrating excellent bonding between the coating and the substrate without

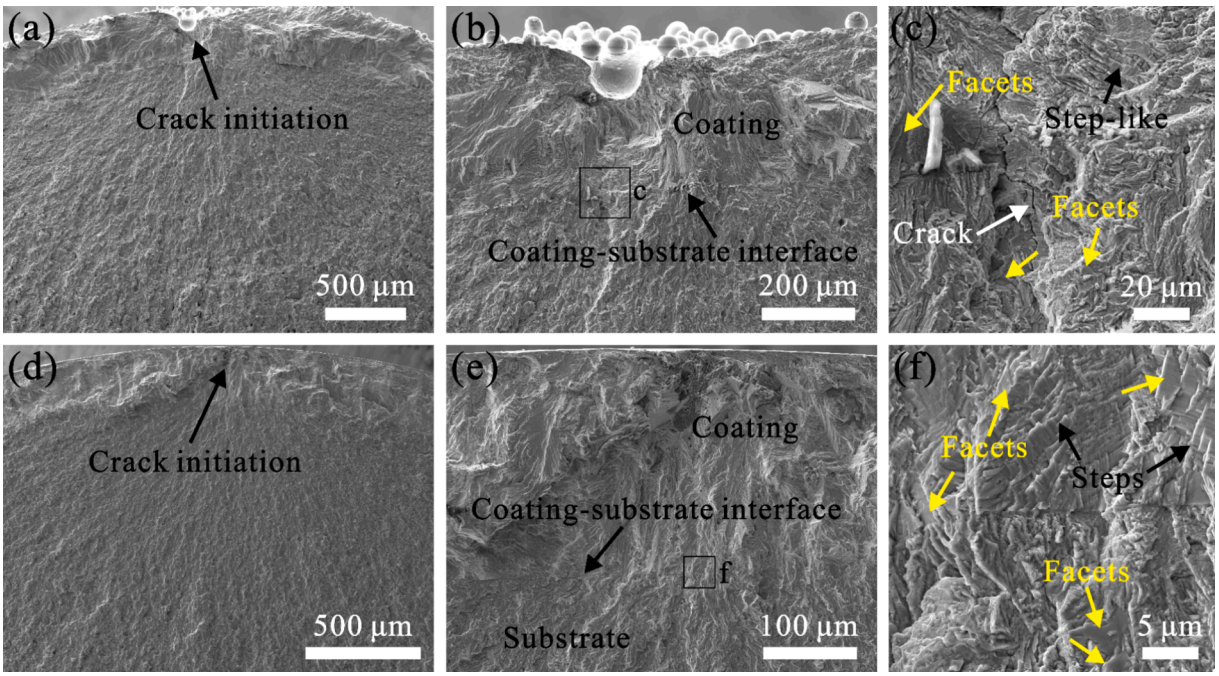

Fig. 14. Single-layer coated specimens fatigue fracture: (a-c) As-deposited specimen: σ_{max} = 350 MPa, N_f = 601,237; (d-f) Surface-polished specimen: σ_{max} = 370 MPa, N_f = 1,959,371.

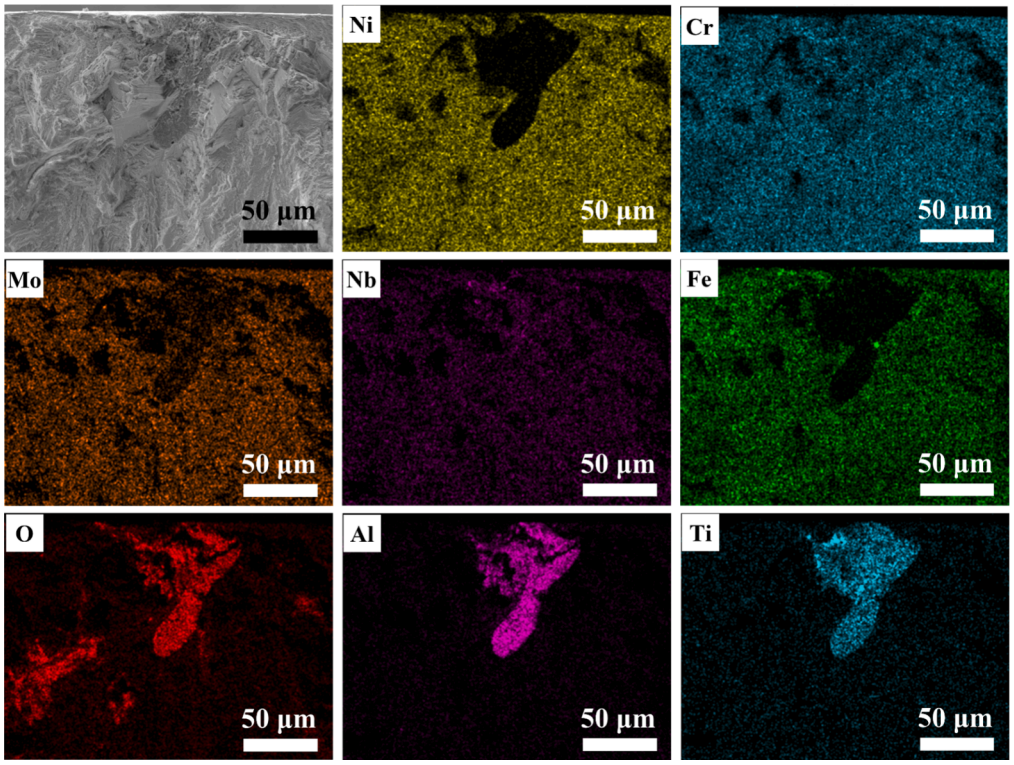

Fig. 15. EDS mapping of single-layer coated specimen fatigue crack initiation.

any observable defects such as delamination or cracks. Similarly, Fig. 9 (b) shows the double-layer coated specimen, demonstrating robust bonding between the substrate and the first layer, as well as between the first and the second layers. Rapid cooling during solidification creates a significant temperature gradient within the molten pool, leading to distinct microstructure at the top, middle, and bottom regions of the coating [43,44]. At the coating top region, unmelted powder particles act as nucleation sites for solidification, resulting in the radial formation of fine dendrites around the unmelted powder, as depicted in Fig. 9(c). The heat input for melting is transferred by conduction along the thickness of the material [45]. This preferential heat dissipation direction leads to a predominantly columnar structure in the coating middle region, as shown in Fig. 9(e), with the columnar growth direction typically being perpendicular to the adjacent fusion zones.

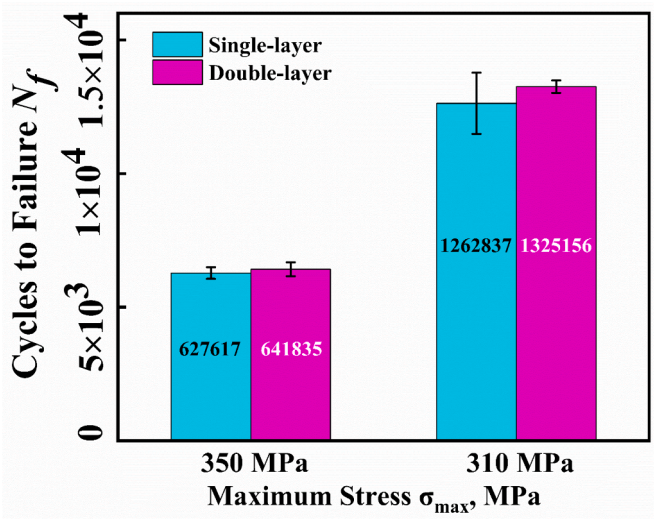

Fig. 16. The fatigue life of the single-layer and double-layer coated as-deposited specimens tested at 350 MPa and 310 MPa maximum stress.

In the coating bottom region, the powders and substrate material undergo melting and subsequent solidification, forming a good bond between the coating and the substrate. Given substantial chemical and physical dissimilarities between the coating and substrate materials, the coating-substrate interface is quite visible in Fig. 9(g) and (h). Conversely, the differences are minimal between the first and the second layers, which are the same alloy and completely blend into each other, resulting in a more uniform bond without a distinct interface between the first and second layers in Fig. 9(f). Fig. 9(f) demonstrates epitaxial columnar crystals growth across the melt pool boundary. This crystals epitaxial growth was also observed in other nickel-based alloy coatings [46]. Despite the absence of a distinct interface between the first and the second layers, their microstructure is notably different. This is primarily due to extensive interdiffusion between the first layer and the substrate, leading to higher iron content in the first layer compared to the second layer. Under similar metallographic corrosion conditions, the first layer with higher iron content experiences more severe corrosion, thus displaying a more pronounced microstructure. At the coating second layer top region, although it consists of fine equiaxed and dendritic crystals in Fig. 9(d), its superior corrosion resistance results in shallower corrosion under similar conditions, rendering less distinct microstructure compared with Fig. 9(c).

EBSD results, inverse pole figure (IPF), grain boundary map and grains size distribution for single-layer and double-layer coated specimens are presented in Fig. 10. Fig. 10(a) and (b) are the IPF and grain boundary maps of the coating and the substrate. The coating primarily composed of columnar grains with an average short-axis width of about 30 μm, significantly larger than the approximately 12 μm equiaxed grains in the substrate. Notably, the HAZ exhibits a noticeable difference in grain size between the single-layer and double-layer coated specimens. The average grain width measured by the transverse method represents the average grain size in Fig. 10(c).

In the HAZ of the single-layer coated specimen, the average grain size measures 12 μm, decreasing with distance from the coating-substrate interface towards the substrate. Grain growth is typically affected by temperature, which decreases continuously from the coating-substrate interface towards the substrate [47,48]. Therefore, the largest grain size within the HAZ is near the coating-substrate interface and diminishes with distance from this boundary. According to the measurements in Fig. 10(c), the grain size in the HAZ of the double-layer coated specimen averages 6 μm, which is smaller than the single-layer specimen. Repeated laser exposure raises the HAZ temperature to the phase transition temperature, inducing a solid-state phase transformation in the HAZ [45]. In the double-layer coated specimen, continuous deposition of the first and second layers leads to heat accumulation in the HAZ, reaching the austenite transition temperature [49]. Subsequently, the coated specimen naturally cools in air, equivalent to normalizing the substrate HAZ of the double-layer coated specimens, thus forming a fine-grained region in the HAZ. However, the single-layer coated specimen's

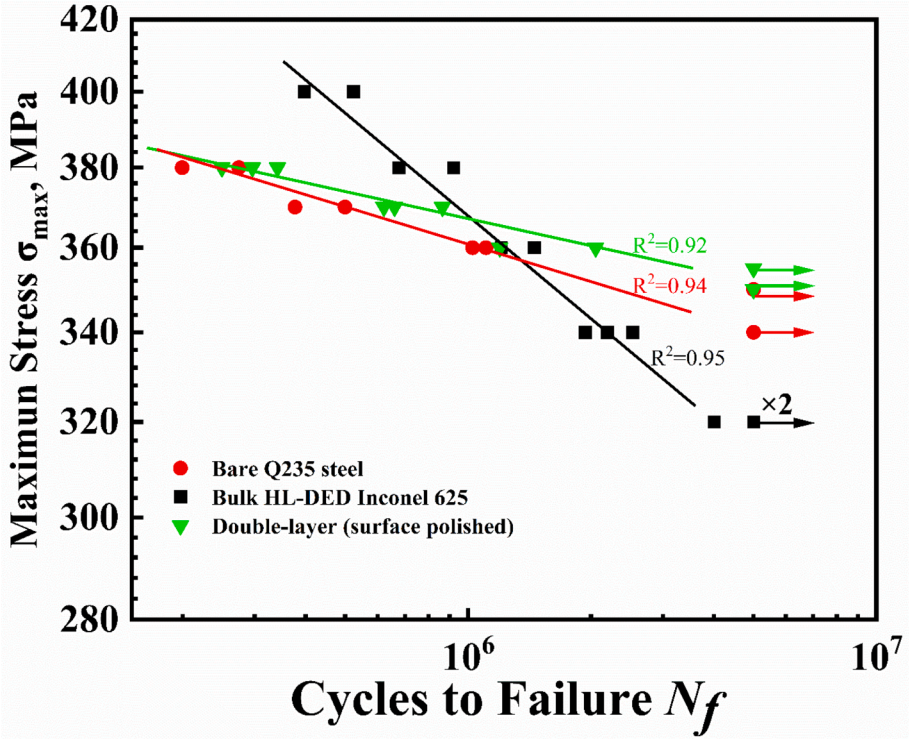

Fig. 17. Fatigue S-N curves for double-layer coated surface polished specimens compared to bare Q235 steel and bulk HL-DED Inconel 625.

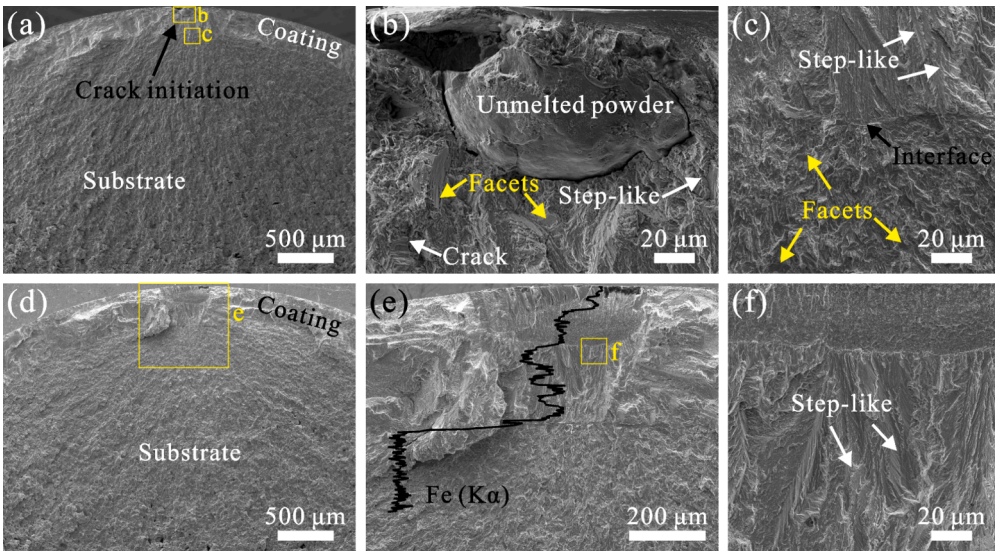

Fig. 18. Fatigue fracture of double-layer coated surface polished specimens: (a-c): σ_{max} = 370 MPa, N_f = 660,474; (d-f): σ_{max} = 360 MPa, N_f = 2,051,404.

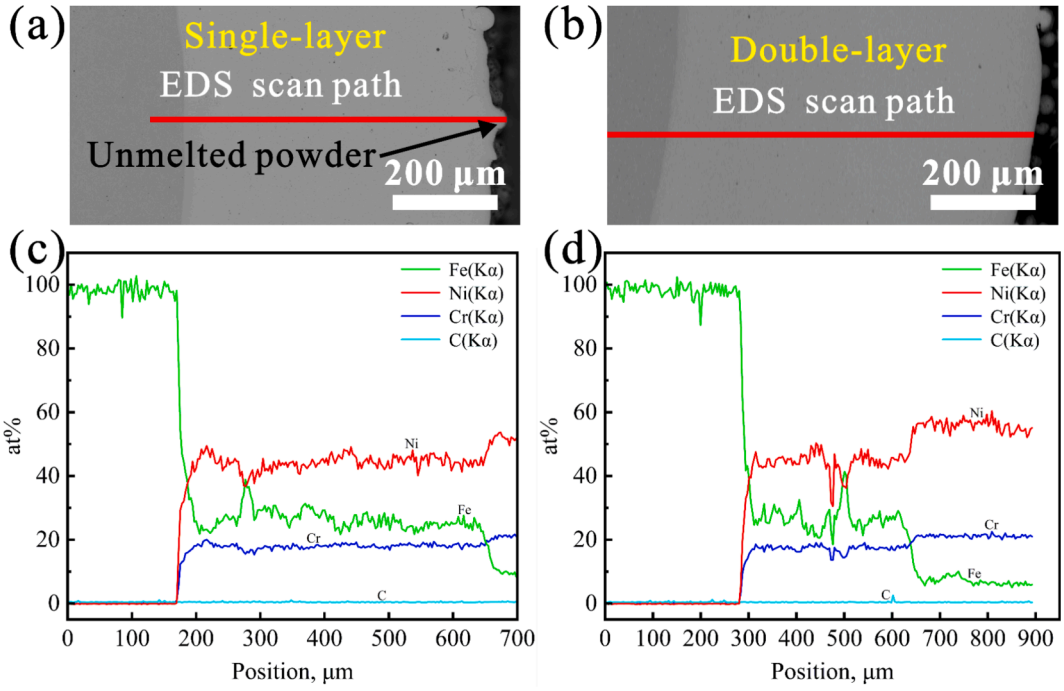

Fig. 19. EPMA analysis of element distribution: (a) and (c) Single-layer coated specimen; (b) and (d) Double-layer coated specimen.

substrate HAZ temperature did not reach the austenite transition temperature, so the single-layer coated specimen substrate HAZ grains only grew resulting in the double-layer coated specimens HAZ grains being smaller than the single-layer.

3.4. Fatigue S-N curves and fracture

3.4.1. Bare Q235 steel and bulk HL-DED Inconel 625 fatigue tests

Bare Q235 steel and bulk HL-DED Inconel 625 specimens serve as reference for the S-N curves comparison with the HL-DED Inconel 625 coated specimens fatigue tests. Despite bulk HL-DED Inconel 625 having higher tensile strength than bare Q235 steel, its fatigue life is shorter at maximum stresses below 350 MPa in Fig. 11, where arrows indicate specimens tested to 5,000,000 cycles without failure and the × 2 mark indicates two specimens. Bulk HL-DED Inconel 625, with higher tensile strengths than bare Q235 steel, better resists permanent deformation and fracture, resulting in a longer fatigue life under high stress. Sandhu's research supports that higher strength materials exhibit longer fatigue life under high stress [22]. However, internal defects in bulk HL-DED Inconel 625 can act as fatigue cracks initiation points, reducing its fatigue life. In contrast, bare Q235 steel has fewer defects and greater plasticity. This property allows it to effectively distribute external stresses during cyclic loading, minimizing local stress concentrations. As a result, it reduces the crack initiation likelihood, demonstrating better fatigue performance in low stress situations.

For the bare Q235 steel specimen, fatigue cracks initiated from a surface inclusion and radiate inward from the crack source, as shown in Fig. 12(a). This radial crack propagation pattern is a typical ductile fracture feature. Further magnification of the crack initiation and propagation region is shown in Fig. 12(b), we observe small facets

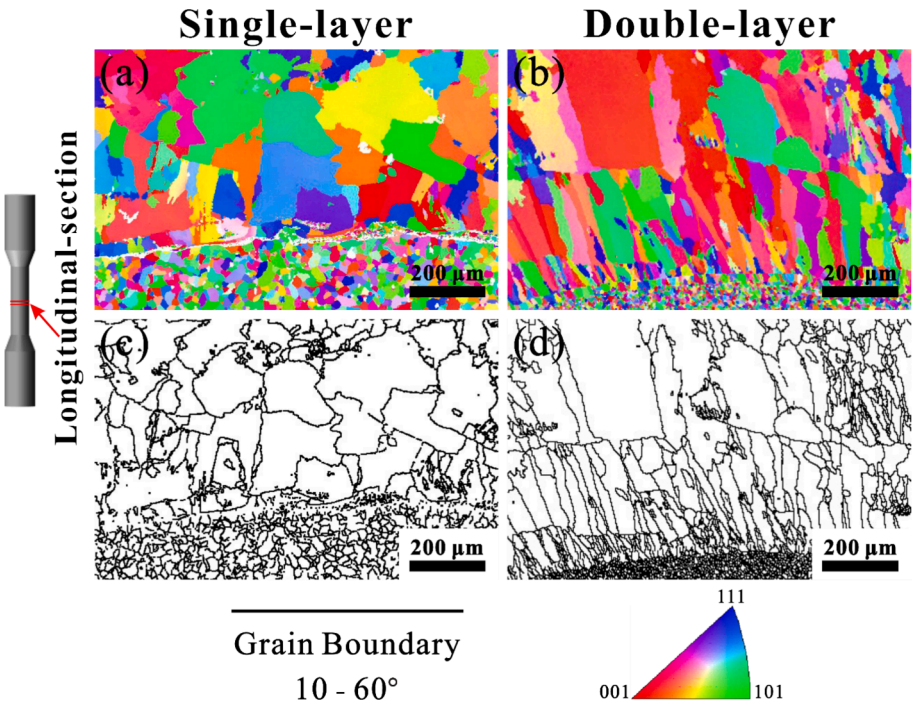

Fig. 20. EBSD results of the coating specimens longitudinal-section: (a) Single-layer coating IPF map, (b) Double-layer coating IPF map; (c) Single-layer coating grain boundaries; (d) Double-layer coating grain boundaries.

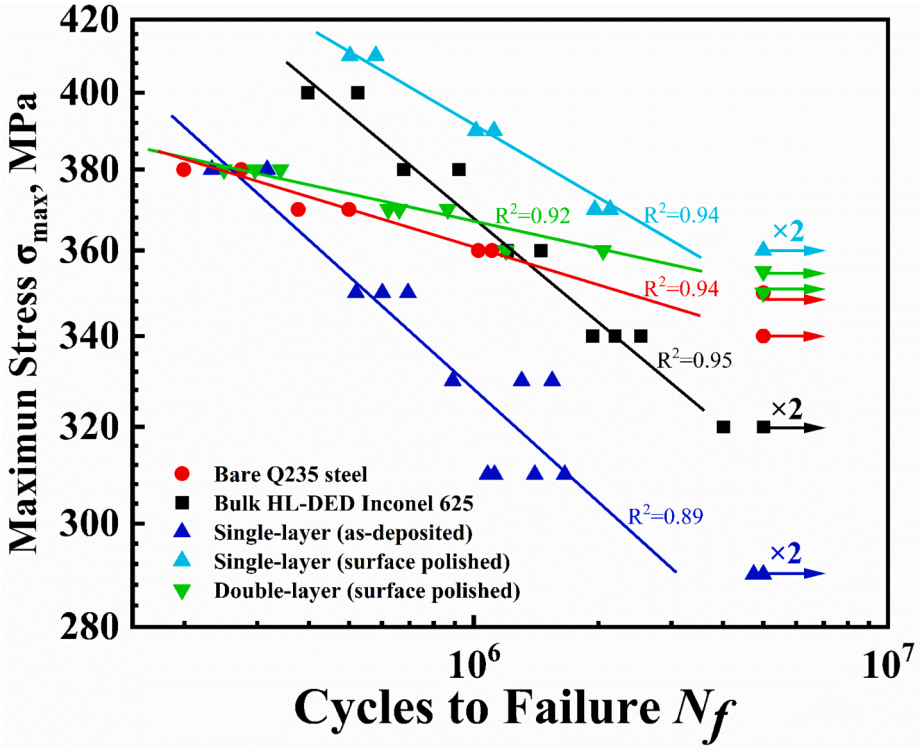

Fig. 21. Fatigue S-N curves for bare Q235 steel, bulk HL-DED Inconel 625 and coated specimens.

characteristic of brittle fracture in the crack propagation region. The final fracture region, as shown in Fig. 12(c), consists of dimples, and its characteristics are similar to those of the tensile fracture. In contrast, for the bulk HL-DED Inconel 625 specimens, fatigue crack initiation and propagation occurred at debonding defects in Fig. 12(d), with a clear image of the initiation region in Fig. 12(e). These defects in the bulk HL-DED Inconel 625 specimens contributed to premature fatigue failure. Additionally, Fig. 12(e) clearly shows that the crack propagation region exhibits a distinct river pattern and step-like features. During fatigue, cracks may preferentially propagate along specific planes, forming small facets. When these facets stack together, they create the step-like features depicted in Fig. 12(e), with each step representing once crack

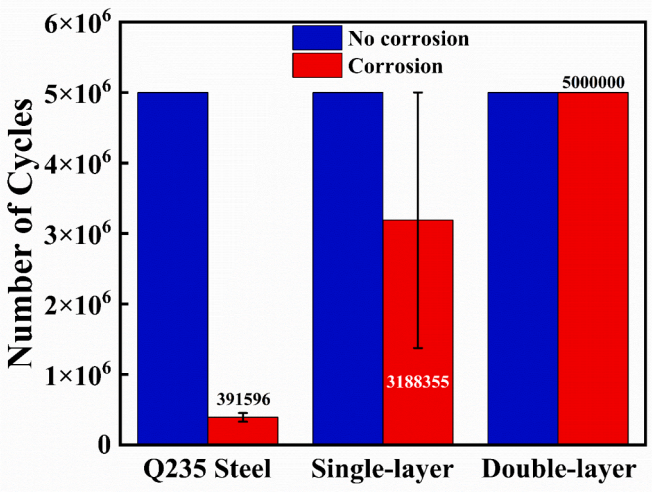

Fig. 22. Corrosion fatigue of bare Q235 steel, single-layer and double-layer coated polished specimens was tested at a 350 MPa maximum stress in a 3.5 % NaCl solution.

propagation. Fig. 12(f) displays the final fracture region of the bulk HL-DED Inconel 625 specimen, which smaller dimples compared to those observed in Fig. 12(c) for Q235 steel. This observation is consistent with Fig. 6(f), where the Inconel 625 coating also exhibits smaller dimples than the Q235 steel.

3.4.2. *Single-layer coated specimens fatigue tests*

The diameter of the as-deposited single-layer specimen is about 8.6 mm. To eliminate the impact of surface unmelted or semi-molten powder on fatigue properties, the polished sample's diameter is 8.3 mm. The fatigue performance of single-layer coated specimens, both in as-deposited and polished conditions, is depicted alongside bulk HL-DED Inconel 625 and bare Q235 steel results in Fig. 13. As-deposited specimens show a notable decrease in fatigue life compared to the bulk HL-DED Inconel 625 and bare Q235 steel. However, when the as-deposited specimen surface is polished, fatigue performance improved significantly, surpassing both bulk HL-DED Inconel 625 and bare Q235 steel. Local surface discontinuities can cause stress concentration and crack initiation, significantly diminishing the fatigue life of as-deposited specimens. In contrast, the coated specimens surface polishing demonstrate increased fatigue life, consistent with Renzo's experimental findings [50].

In the as-deposited coated specimens, the presence of semi-melted and unmelted powder on the surface is the primary factor contributing to reduced fatigue lifetime. Fig. 14(a) shows fatigue crack initiation from surface pore defects in the as-deposited condition, with the defect clearly visible in Fig. 14(b). These pore defects, which are not accounted for in dimensional measurements, increase the actual stress in the tested specimen due to the reduced transverse-section area. Additionally, the pore causes higher stress concentration, facilitating fatigue crack initiation [51]. However, the crack initiation stage is critical in the high-cycle fatigue process, accounting for 90 % of the fatigue life [52]. Fig. 14(c) shows secondary cracks extending from the coating into the substrate, along with small facets in the crack propagation region. After polishing, the semi-melted and unmelted powder particles on the as-deposited surface are completely removed, resulting in a smoother surface. Fig. 14(d) shows fatigue crack initiation from the inclusions of coating surface in the polished specimen, with a clear view of the crack initiation zone in Fig. 14(e). The crack propagation region of the polished specimens also exhibits facets and step-like features, as shown in Fig. 14(f). EDS analysis results of the crack initiation zone are shown in Fig. 15, revealing inclusions rich in O, Al, and Ti elements. These inclusions promote the initiation and propagation of fatigue cracks.

3.4.3. *Double-layer coated specimens fatigue tests*

At the as-deposited condition, the diameter of the single-layer coating specimen is approximately 8.6 mm, while the double-layer coating specimen is about 8.9 mm. Although the double-layer coating is thicker, the difference is minimal. The fatigue performance of double-layer coated specimens in the as-deposited condition was tested at two stress levels, 350 MPa and 310 MPa in Fig. 16. At the identical stress levels, the fatigue life of single-layer and double-layer coated specimens in the as-deposited condition showed no significant difference. This can be attributed to the fact that surface defects such as semi-melted and unmelted powder are prevalent in the as-deposited condition. These surface defects will promote fatigue cracks initiation. Additionally, the YS and UTS of double-layer coated specimens is only 25 MPa higher than the single-layer coated specimens, and their elongation is reduced by 2 %. The combined effect of increased strength and decreased plasticity results in no notable difference in fatigue properties between the single-layer and double-layer coated specimens in the as-deposited condition. Under the combined influence of these factors, there is no distinction in the fatigue life of single-layer and double-layer coated specimens at the as-deposited condition.

After polishing, the double-layer coating thickness is 8.6 mm. Fig. 17 displays the S-N curves for double-layer coated polished specimens. The fatigue performance of the double-layer coated specimen is comparable to that of bare Q235 steel. Although the ultimate tensile strength of the double-layer coated specimen increases by 27 % compared to bare Q235 steel, the elongation decreased by 39 %. This is likely due to the balance between increased strength and reduced plasticity, which results in minimal differences in fatigue performance between the double-layer coated specimen and bare Q235 steel.

Defects introduced at the interlayer interface are a primary cause of fatigue crack initiation, as reported by Doubek [53]. However, we observed that fatigue cracks can still initiate at this interface even in the absence of defects. Fig. 18 illustrates the fatigue failure characteristics of double-layer coated polished specimens, where cracks initiate at the surface defects and coating interfaces. Fig. 18(a) and (b) show that incomplete melting of powder in the coating can serve as a fatigue crack initiation point. Additionally, many small facets and step-like morphologies can be seen near the coating region, as shown in Fig. 18(b) and (c). The crack propagation morphology in the substrate resembles that of bare Q235 steel, as shown in Fig. 18(c). Furthermore, in defect-free coating specimens, cracks initiate from the interlayer interface in Fig. 1 8(d) and (e). The low iron content in Inconel 625 compared to the Q235 steel causes iron migration into the coating during the HL-DED process, leading to increased iron content in the coating first layer. The interlayer interface in the fracture zone can be accurately identified by analyzing the variation in iron content. In Fig. 18(e) EDS line scanning reveals a stepwise decrease in iron content across the substrate, coating first and second layers. Despite the difference in crack initiation between Fig. 18(d) and Fig. 18(a), the crack propagation morphology in the coating exhibits similar characteristics, primarily consisting of small facets and step-like features, as shown in Fig. 18(c) and (f). This indicates that while the initial crack formation mechanism may differ, the crack propagation mechanism is the same.

For better understanding the cause of crack initiation at the coating interface, longitudinal-section elements were analyzed using EPMA. Fig. 19(a) and (b) depict the EPMA line scan position, and the analysis results are presented in Fig. 19(c) and (d). It is evident in Fig. 19(d) that the carbon content at the interface between the coating first and second layers is significantly increased. This abnormal rise in carbon content suggests the formation of carbides at the interface. Carbides are recognized as hard and brittle phases that can induce stress concentrations under cyclic loading, thereby promoting crack initiation at these sites [54]. Additionally, EBSD results from the longitudinal-section in Fig. 20 reveal that the double-layer coated specimen displays pronounced columnar grains and distinct large-angle grain boundaries at the interface between the first and second coating layers. Large-angle grain

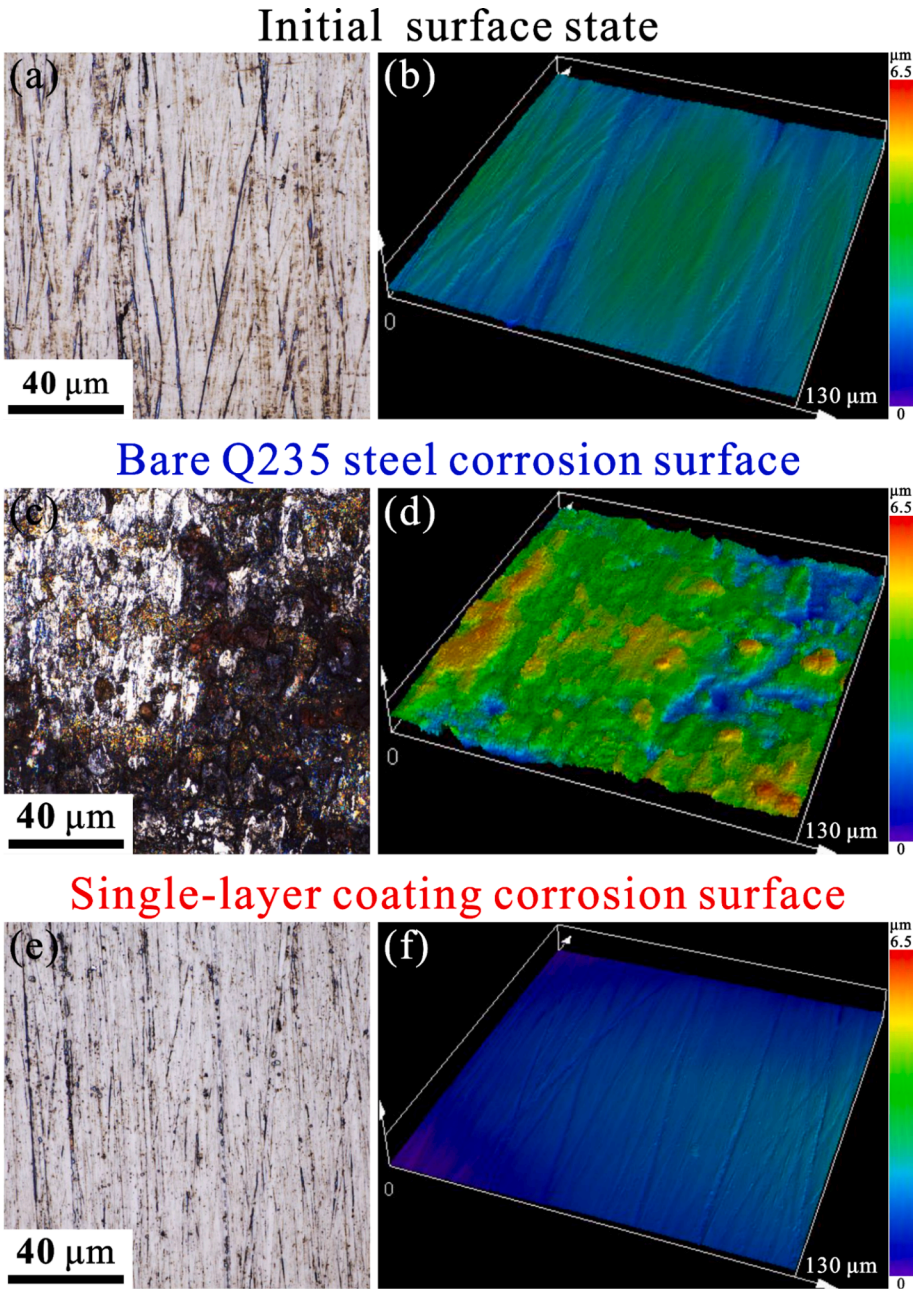

Fig. 23. Initial state and corrosion fatigue failure specimens surface topography were analyzed by laser confocal microscopy: (a) and (b) Initial surface state; (c) and (d) Bare Q235 steel corrosion surface; (e) and (f) Single-layer coated corrosion surface.

boundaries are high-energy regions with a significant lattice mismatch and discontinuities, making them effective sites for carbide precipitation and lowering the energy barrier for carbide nucleation. It is well-established for nickel-based alloys that carbides readily precipitate at large-angle grain boundaries [55]. However, the presence of carbides introduces stress concentrations at grain boundaries. Under cyclic loading, these stress concentrations initiate cracks, which propagate along the grain boundaries, ultimately leading to material fatigue failure. This explanation is supported by the crack initiation morphology in Fig. 18(d).

The fatigue S-N curves for bare Q235 steel, bulk HL-DED Inconel 625 and coated specimens are presented in Fig. 21 to summarize the comprehensive evaluation of fatigue performance across different specimen types. As-deposited coating specimens demonstrate the worst fatigue performance, with no significant impact observed by varying coating thickness. In contrast, polished coating specimens show significant improvements in fatigue performance, although their fatigue life decreases with the coating thickness. This phenomenon can be attributed to the higher residual tensile stress in thicker coatings, which negatively impacts fatigue performance and reduce fatigue life, as reported by Hutasoit et al. [18]. Fatigue properties negatively correlate with coating thickness also observed in thermal spray coatings. As coating thickness increases, defect size also grows, leading to reduced fatigue strength [21].

3.5. *Corrosion fatigue tests*

The corrosion fatigue test results highlight the primary objective of applying Inconel 625 coating to the Q235 steel surface to enhance corrosion resistance. Fatigue tests were conducted using bare Q235 steel and polished coated specimens immersed in a 3.5 % NaCl solution in Fig. 22. Under no corrosion conditions, both bare Q235 steel and the

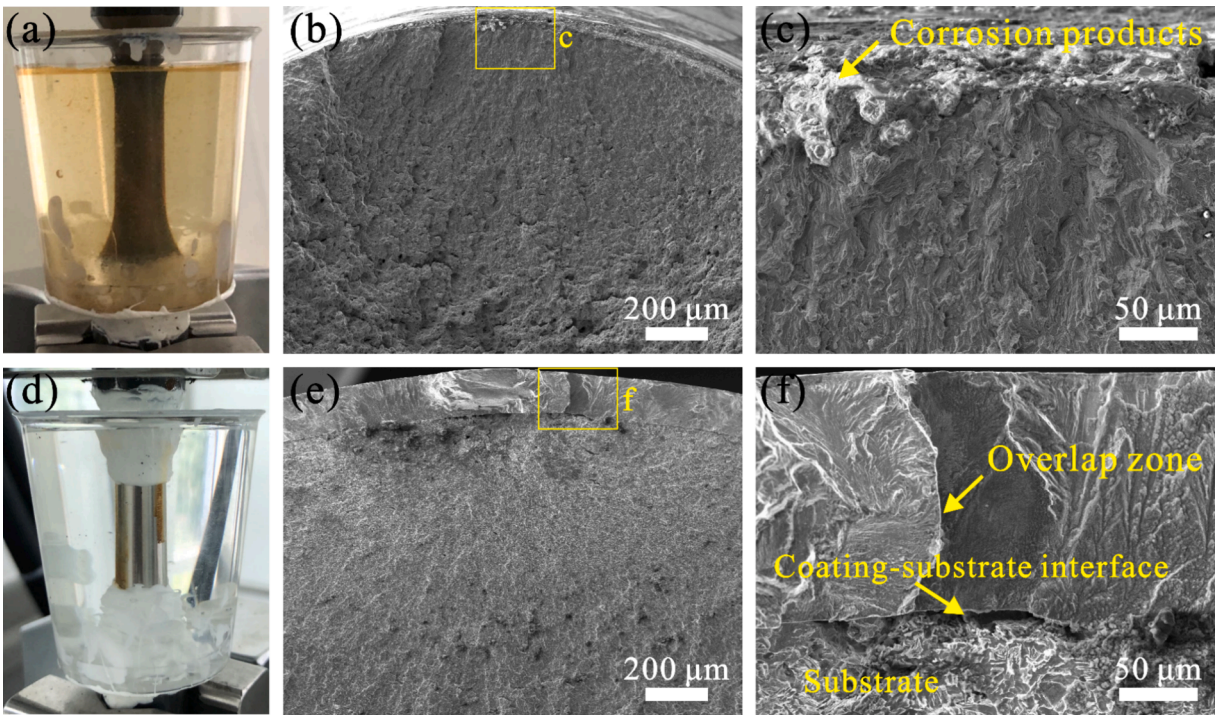

Fig. 24. Corrosion fatigue fracture morphology: (a-c) Bare Q235 steel: σ_{max} = 350 MPa, N_f = 329,765; (d-f) Single-layer coated surface polished specimen: σ_{max} = 350 MPa, N_f = 1,376,709.

coated specimens sustained 5,000,000 cycles without fracture at 350 MPa maximum stress. However, when exposed to corrosive environment, bare Q235 steel specimens experienced fatigue fracture. Between the two single-layer coated specimens, one experienced fatigue fracture after 1,376,709 cycles, while the other did not fracture even after 5,000,000 cycles. However, the two double-layer coated specimens endured 5,000,000 cycles without fracture. Despite the corrosion fatigue failure of the single-layer coated specimen, its corrosion fatigue life was still higher than bare Q235 steel under the same maximum stress. This is in stark contrast to the decreased corrosion fatigue performance observed in Inconel 625 coatings produced by high velocity oxy fuel spraying. Although Inconel 625 offers excellent corrosion resistance, the interconnected porosity of high velocity oxy fuel coatings allows corrosive media to penetrate and attack the substrate, diminishing their corrosion fatigue performance [56]. These findings highlight the advantages of using high-speed laser deposition for Inconel 625 coatings, which effectively protects substrate from corrosion.

Fig. 23 illustrates the surface topography of specimens in their initial state and after corrosion fatigue failure, examined using a laser confocal microscope. In the initial state, the specimen surface displays regular machining marks in Fig. 23(a), and the surface roughness map in Fig. 23 (b) indicates a relatively smooth surface. After exposure to a 3.5 % NaCl solution, bare Q235 steel exhibits eroded marks and significant corrosion pits on the surface in Fig. 23(c). The corresponding surface roughness map in Fig. 23(d) shows a notably roughened surface, demonstrating the destructive impact of corrosion on the bare Q235 steel surface. Despite the reduced fatigue life of single-layer coated specimens in the corrosive environment, their endurance time exceeds bare Q235 steel by more than threefold. Examination of the specimen surfaces reveals minimal signs of corrosion, indicating that the Inconel 625 coating offers robust corrosion resistance in the 3.5 % NaCl solution in Fig. 23(e) and (f).

Fig. 24(a) shows severe corrosion of bare Q235 steel after 5 h of fatigue in a 3.5 % NaCl solution. Fig. 24(b) and (c) depict the corrosion fatigue fracture surfaces of bare Q235 steel. Multiple cracks originating from the surface are visible in Fig. 24(b). A closer view of the crack initiation zone is shown in Fig. 24(c), where abundant white corrosion products cover the area, indicating substantial corrosive damage to the bare Q235 steel surface. In contrast, the single-layer coated polished specimen experienced minimal corrosion, confined to a single spot on its surface in Fig. 24(d). Fig. 24(e) and (f) show the corrosion fatigue fracture of a single-layer coated surface polished specimen. In Fig. 24(e), the edges of the coated sample fracture surface appear relatively clean, without corrosion pits in Fig. 24(b). However, distinct voids are observed at the junction between the Inconel 625 coating and the substrate in the corrosion fatigue crack initiation zone, which are absent in no corrosion fatigue fractures. A magnified view of the fatigue initiation zone in Fig. 24(e) is shown in Fig. 24(f), where a step can be observed at the boundary between bright and dark regions, indicating a non-planar fracture surface, likely related to the overlapping process during laser deposition. At these overlaps, the higher iron content results in reduced corrosion resistance, leading to preferential corrosion in corrosive environments. Once corrosion breaches the overlap and reaches the substrate-coating interface, the protective capability of the coating diminishes, facilitating corrosion pit formation and promoting fatigue failure. In contrast, the second layer exhibits lower iron content compared to the first layer, as evidenced by elemental analysis in Fig. 19 (d). Lower iron content enhances corrosion resistance of Inconel 625 alloy. Therefore, the second layer reduced iron content provides improved corrosion resistance, ensuring that fatigue life is less affected by corrosion damage in corrosive environments.

4. Conclusions

In this study, Inconel 625 coating was applied to the Q235 steel surface using HL-DED. The microstructure of the coating and its effects on tensile and fatigue properties were analyzed. The key findings are summarized as follows:

1. The HAZ grains in the single-layer coated specimen were coarsened, whereas the HAZ in the double-layer coated specimen formed a fine-grain region.

2. Bulk HL-DED Inconel 625 exhibited higher tensile strength compared to bare Q235 steel, but its fatigue limit at 310 MPa was lower than at 350 MPa for bare Q235 steel.
3. HL-DED Inconel 625 coating on the Q235 surface significantly enhanced tensile strength. The thickness of the coating was positively correlated with tensile strength and negatively correlated with elongation.
4. The fatigue strength of the as-deposited coated specimens was lower than bare Q235 steel, but the fatigue strength of the coated surface polished specimens exceeded bare Q235 steel. The coating thickness of the as-deposited coated specimens had minimal effect on fatigue performance, while the fatigue performance of the coated surface polished specimens showed a negative correlation with coating thickness.
5. In a 3.5 % NaCl corrosive environment, the fatigue life of single-layer coated specimens may be reduced, but it remains significantly better than that of bare Q235 at the same stress level. In contrast, the double-layer coated specimen fatigue properties are not affected by the corrosive environment.

CRediT authorship contribution statement

Cheng Zhong: Writing – original draft, Methodology, Investigation, Data curation. **Peng Liu:** Methodology, Investigation, Data curation. **Xuechong Ren:** Writing – review & editing, Project administration, Funding acquisition, Conceptualization. **Benli Luan:** Writing – review & editing, Supervision, Resources. **Alex A. Volinsky:** Writing – review & editing.

Declaration of competing interest

The authors declare that they have no known competing financial interests or personal relationships that could have appeared to influence the work reported in this paper.

Acknowledgments

This work was supported by the Special Project for Industrial Foundation Reconstruction and High Quality Development of Manufacturing Industry [grant number TC220A04W-4]; and the National Natural Science Foundation of China (NSFC) [grant number 11932020].

Appendix A. Supplementary data

Supplementary data to this article can be found online at https://doi.org/10.1016/j.ijfatigue.2024.108746.

Data availability

Data will be made available on request.

References

[1] Wang YT, Feng GQ, Ren HL, Li CF, Lin. Fatigue crack propagation rate test of Q235 steel in ship hull. J Harbin Eng Univ 2015;36:1302–6. https://doi.org/10.1115/omae2015-41501.
[2] Zhang YF, Chen W, Yan HB, Wang XF, Zhang HP, Wu SJ. The effect of atmospheric chloride ions on the corrosion fatigue of metal wire clips in power grids. Atmos 2023;14. https://doi.org/10.3390/atmos14020237.
[3] Xu SH, Qiu B. Experimental study on fatigue behavior of corroded steel. Mater Sci Eng A 2013;584:163–9. https://doi.org/10.1016/j.msea.2013.07.006.
[4] Martin FJ, Natishan PM, Lucas KE, Hogan EA, Grolleau AM, Thomas ED. Crevice corrosion of alloy 625 in natural seawater. Corrosion 2003;59:498–504. https://doi.org/10.5006/1.3277580.
[5] Rajani HR, Mousavi SA, Sani FM. Comparison of corrosion behavior between fusion cladded and explosive cladded Inconel 625/plain carbon steel bimetal plates. Mater Des 2013;43:467. https://doi.org/10.1016/j.matdes.2012.06.053.
[6] Doroudi A, Dastgheib A, Omidvar H. The bonding temperature effect of the diffusion brazing Inconel 625 superalloy on the microstructure changes, corrosion resistance, and mechanical properties. J Manuf Process 2020;53:213–22. https://doi.org/10.1016/j.jmapro.2020.02.005.
[7] Tiago AR, Francisco WCF, Julian AA, Emad M. Effect of heat treatments on Inconel 625 fabricated by wire and arc additive manufacturing: An in situ synchrotron X-ray diffraction analysis. Sci Technol Weld Join 2023;28:534–9. https://doi.org/10.1080/13621718.2023.2187927.
[8] Verdi D, Garrido MA, Múnez CJ, Poza P. Mechanical properties of Inconel 625 laser cladded coatings: Depth sensing indentation analysis. Mater Sci Eng A 2014;598:15–21. https://doi.org/10.1016/j.msea.2014.01.026.
[9] Schopphoven T, Gasser A, Wissenbach K, Poprawe R. Investigations on ultra-high-speed laser material deposition as alternative for hard chrome plating and thermal spraying. J Laser Appl 2016;28. https://doi.org/10.2351/1.4943910.
[10] Li J, Liu Z, Ning H, Ma H, Xie R, Kong Y, et al. Ni-based coating on 5083 aluminum alloy with Cu-Ni interlayer fabricated by ultra-high-speed laser directed energy deposition. Sur Coat Technol 2023;474. https://doi.org/10.1016/j.surfcoat.2023.130068.
[11] Scendo M, Staszewska K, Danielewski H. Corrosion behavior of Inconel 625 coating produced by laser cladding. Coatings 2021:11. https://doi.org/10.3390/coatings11070759.
[12] Abioye TE, McCartney DG, Clare AT. Laser cladding of Inconel 625 wire for corrosion protection. J Mater Process Technol 2015;217:232–40. https://doi.org/10.1016/j.jmatprotec.2014.10.024.
[13] Sun R, Shi Y, Yang Y, Wang X, Zhou X. Microstructure, element segregation and performance of Inconel 625 metal layer deposited by laser assisted ultra-high frequency induction deposition. Sur Coat Technol 2021:405. https://doi.org/10.1016/j.surfcoat.2020.126715.
[14] Rezayat M, AboutorabiA NM, Yazdi M, Taheri M, Moghanian A, et al. Effect of lateral laser-cladding process on the corrosion performance of Inconel 625. Metals 2023;13. https://doi.org/10.3390/met13020367.
[15] Xu X, Mi G, Chen L, Xiong L, Jiang P, Shao X, et al. Research on microstructures and properties of Inconel 625 coatings obtained by laser cladding with wire. J Alloys Compd 2017;715:362–73. https://doi.org/10.1016/j.jallcom.2017.04.252.
[16] Tuominen J, Näkki J, Poutala J, Miettinen J, Peltola T, Vuoristo P, et al. Fatigue behavior of laser clad round steel bars. J Laser Appl 2015;27. https://doi.org/10.2351/1.4903351.
[17] Cheng J, Xing Y, Dong E, Zhao L, Liu H, Chang T, et al. An overview of laser metal deposition for cladding: defect formation mechanisms, defect suppression methods and performance improvements of laser-cladded Layers. Mater 2022;15. https://doi.org/10.3390/ma15165522.
[18] Hutasoit N, Luzin V, Blicblau A, Yan W, Brandt M, Cottam R. Fatigue life of laser clad hardfacing alloys on AISI 4130 steel under rotary bending fatigue test. Int J Fatigue 2015;72:42–52. https://doi.org/10.1016/j.ijfatigue.2014.11.001.
[19] Lourenco JM, Sun SD, Sharp K, Luzin V, Klein AN, Wang CH, et al. Fatigue and fracture behavior of laser clad repair of AerMet 100 ultra-high strength steel. Int J Fatigue 2016;85:18–30. https://doi.org/10.1016/j.ijfatigue.2015.11.021.
[20] Chew YX, Pang JH, Bi GJ, Song B. Effects of laser cladding on fatigue performance of AISI 4340 steel in the as-clad and machine treated conditions. J Mater Process Technol 2017;243:246–57. https://doi.org/10.1016/j.jmatprotec.2016.12.020.
[21] Akebono H. The effect of coating thickness on fatigue properties of steel thermally sprayed with Ni-based selffluxing alloy. Int J Mod Phys 2006;20:3599–604. https://doi.org/10.1142/s0217979206040052.
[22] Sandhu SS, Metallurgical SAS. Wear and fatigue performance of Inconel 625 weld claddings. J Mater Process Technol 2016;233:1–8. https://doi.org/10.1016/j.jmatprotec.2016.02.010.
[23] Kumar NP, Shanmugam NS, Sreedhar G. High cycle fatigue behaviour of Inconel 625 weld overlay on AISI 316L plate. Sur Coati Technol 2021::415. https://doi.org/10.1016/j.surfcoat.2021.127138.
[24] Zhong C, Ren XC, Fu K, Luan BL. Effect of Thermal Aging on the Microstructure and Mechanical Properties of Inconel 625 Superalloy Fabricated by High-Speed Laser Metal Deposition. Metall Mater Trans B 2023;54:2723–36. https://doi.org/10.1007/s11663-023-02869-3.
[25] Administration of Quality Supervision, Inspection and Quarantine of People's Republic of China, Standardization Administration of China, GB/T 228.1–2010 Metallic Materials - Tensile Testing - Part 1: Method of Test at Room Temperature. China Standards Press, Beijing, 2010 (in Chinese).
[26] Administration of Quality Supervision. Inspection and Quarantine of People's Republic of China, Standardization Administration of China, GB/T 3075–2008 Metallic materials—Fatigue testing—Axial-force-controlled method. Beijing: China Standards Press; 2008. in Chinese.
[27] Gui WY, Zhong C, Gu JY, Ding YH, Wang XM, Wu T, Qin,. Qu YH, Lin JP. Laser-clad Inconel 625 coatings on Q245R structure steel: microstructure, wear and corrosion resistance. npj Mater Degrad 2022:6. doi: 10.1038/s41529-022-00247-z.
[28] Wu Y, Wu X, Li L, Li B, Wang Z. Modeling of process parameters and wear performance investigation of Inconel 625 nickel-based coatings via laser cladding. Opt Laser Technol 2025:181. https://doi.org/10.1016/j.optlastec.2024.111749.
[29] Administration of Quality Supervision. Inspection and Quarantine of People's Republic of China, Standardization Administration of China, GB/T 27552–2011Destructive tests on welds in metallic materials—Microhardness testing of welded joints. Beijing: China Standards Press; 2011. in Chinese.
[30] Nonaka I, Setowaki S, Ichikawa Y. Effect of load frequency on high cycle fatigue strength of bullet train axle steel. Int J Fatigue 2014;60:43–7. https://doi.org/10.1016/j.ijfatigue.2013.08.020.

[31] Huang CY, Hai LT, Jiang JB, Ban HY. High-cycle fatigue properties of explosion bonded titanium-clad bimetallic steel. Int J Fatigue 2023;169. https://doi.org/10.1016/j.ijfatigue.2022.107499.
[32] He X, Yan Z, Liang H, Wang D. Corrosion fatigue acoustic emission characteristics and evaluation of friction stir welding joints of AZ31 magnesium alloy in 3.5 wt.% NaCl solution. J Mater Res Technol 2023;25:4582–94. https://doi.org/10.1016/j.jmrt.2023.06.240.
[33] Verdi D, Múnez CJ, Garrido MA, Poza P. Process parameter selection for Inconel 625-Cr3C2 laser cladded coatings. Int J Adv Manuf Technol 2017;92:3033–42. https://doi.org/10.1007/s00170-017-0372-4.
[34] Shayanfar P, Daneshmanesh H, Janghorban K. Parameters optimization for laser cladding of Inconel 625 on ASTM A592 steel. J Mater Res Technol 2020;9:8258–65. https://doi.org/10.1016/j.jmrt.2020.05.094.
[35] Guo L, Cui L, Xiao F, Xu B, Wu Z, Cao Y, et al. Influence of process parameters on surface properties and corrosion resistasnce of Inconel 625 coating prepared by laser cladding. Int J Electrochem Sci 2023;18. https://doi.org/10.1016/j.ijoes.2023.100213.
[36] Lou D, Yang S, Mei S, Liu Q, Cheng J, Yang Q, et al. The effect of laser scanning speed on microstructure and performance of Cr_3C_2-NiCr cermet fabricated by in-situ laser cladding. Mater Sci 2021;27:167–74. https://doi.org/10.5755/j02.ms.23557.
[37] Zhao Y, Yu T, Sun J, Chen L, Chen Y. Effect of laser cladding on forming microhardness and tensile strength of YCF101 alloy powder in the different full lap joint modes. J Alloys Compd 2020;820. https://doi.org/10.1016/j.jallcom.2019.04.046.
[38] Åhman HN, Larsson L, Wahman C, Mellin P, D'Elia F, Persson C. Higher laser power improves strength but reduces corrosion resistance of Mg WE43 processed by powder bed fusion. Mater Today Commun 2024;39. https://doi.org/10.1016/j.mtcomm.2024.108979.
[39] Wang X, Liu Z, Li J, Chen L, Li B. Effect of heat treatment on microstructure, corrosion resistance, and interfacial characteristics of Inconel 625 laser cladding layer. Optik 2022;270. https://doi.org/10.1016/j.ijleo.2022.169930.
[40] Wang Z, Peng B, Ning H, Zhang J, Han Z, Li J. Effect of Si on the mechanical properties of Inconel 625 laser cladding layer. Mater Lett 2024;354. https://doi.org/10.1016/j.matlet.2023.135380.
[41] Zhang M, Guo Y, Guo Z, Zhang L, Wang G, Li B. Microstructure evolution simulation of laser cladding process based on CA-FD model. Cryst Res Technol 2021;56. https://doi.org/10.1002/crat.202100050.
[42] Fu K, Zhong C, Zhang L, Wang XM, Nie BX, Xue YP, et al. Effect of multiple thermal cycling on the microstructure and microhardness of Inconel 625 by high-speed laser cladding. J Mater Res Technol 2023;24:1093–107. https://doi.org/10.1016/j.jmrt.2023.03.064.
[43] Ferreira AA, Amaral RL, Romio PC, Cruz JM, Reis AR, Vieira MF. Deposition of Nickel-based superalloy claddings on low alloy structural steel by direct laser deposition. Metals 2021:11. https://doi.org/10.3390/met11081326.
[44] Wang QY, Pei R, Liu S, Wang SL, Dong LJ, Zhou LJ, et al. Microstructure and corrosion behavior of different clad zones in multi-track Ni-based laser-clad coating. Sur Coat Technol 2020;402. https://doi.org/10.1016/j.surfcoat.2020.126310.
[45] Shen JJ, Yeon TC, Yang J, He JJ, Zeng Z, Oliveira JP. Fabrication of spatially-variable heterostructured CoCrFeMnNi high entropy alloy by laser processing. Mater Sci Eng A 2024;896. https://doi.org/10.1016/j.msea.2024.146272.
[46] Li W, Sugio K, Liu X, Yamamoto M, Guo Y, Zhu S, et al. Microstructure evolution and mechanical properties of 308L stainless steel coatings fabricated by laser hot wire cladding. Mater Sci Eng A 2021;824. https://doi.org/10.1016/j.msea.2021.141825.
[47] Yogo Y, Tanaka K, Ikehata H, Iwata N, Nakanishi K, Ishikawa T. The solute drag model to calculate grain growth rate at high temperatures in carbon steels. Mater Sci Foru 2012;706–709:1574–9. https://doi.org/10.4028/www.scientific.net/MSF.706-709.1574.
[48] Gao J, Wu C, Hao Y, Xu X, Guo L. Numerical simulation and experimental investigation on three-dimensional modelling of single-track geometry and temperature evolution by laser cladding. Opt Laser Technol 2020;129. https://doi.org/10.1016/j.optlastec.2020.106287.
[49] Zhou S, Xu T, Hu C, Wu H, Liu H, Ma X. Effect of different topologies on microstructure and mechanical properties of multilayer coatings deposited by laser cladding with Inconel 625 wire. Sur Coat Technol 2021;421. https://doi.org/10.1016/j.surfcoat.2021.127299.
[50] Renzo DA, Maletta C, Sgambitterra E, Furgiuele F, Berto F. Surface roughness effect on multiaxial fatigue behavior of additively manufactured Ti6Al4V alloy. Int J Fatigue 2022;163. https://doi.org/10.1016/j.ijfatigue.2022.107022.
[51] Alam MM, Kaplan AF, Tuominen J, Vuoristo P, Miettinen J, Poutala J, et al. Analysis of the stress raising action of flaws in laser clad deposits. Mater Des 2013;46:328–37. https://doi.org/10.1016/j.matdes.2012.10.010.
[52] Martin N, Hor A, Copin E, Lours P, Ratsifandrihana L. Fatigue properties of as-built and heat-treated Inconel 625 obtained by the hybridization of two laser-powder based additive processes. Int J Fatigue 2023;172. https://doi.org/10.1016/j.ijfatigue.2023.107650.
[53] Doubek P, Kozáková K, Kunz L, Seitl S. Fatigue life of S960 high strength steel with laser cladded functional surface layers. Eng Fail Anal 2024;164. https://doi.org/10.1016/j.engfailanal.2024.108629.
[54] Lee T-H, Lee Y-J, Joo S-H, Nersisyan HH, Park K-T, Lee J-H. Intergranular $M_{23}C_6$ carbide precipitation behavior and Its effect on mechanical properties of Inconel 690 tubes. Metall Mater Trans A 2015;46:4020–6. https://doi.org/10.1007/s11661-015-3003-4.
[55] Dong X, Zhang X, Du K, Zhou Y, Jin T, Ye H. Microstructure of carbides at grain boundaries in nickel based superalloys. J Mater Sci Technol 2012;28:1031–8. https://doi.org/10.1016/s1005-0302(12)60169-8.
[56] Al-Fadhli HY, Stokes J, Hashmi MSJ, Yilbas BS. HVOF coating of welded surfaces: Fatigue and corrosion behaviour of stainless steel coated with Inconel-625 alloy. Sur Coat Technol 2006;200:4904–8. https://doi.org/10.1016/j.surfcoat.2005.04.052.